

---

# Simultaneous detection of flare-associated kink oscillations and extreme-ultraviolet waves<sup>\*</sup>

Dong Li<sup>1,2</sup>, Zhenyong Hou<sup>3</sup>, Xianyong Bai<sup>4,5</sup>, Chuan Li<sup>6,7</sup>, Matthew Fang<sup>8</sup>, Haisheng Zhao<sup>9</sup>, Jincheng Wang<sup>2,10</sup>, and Zongjun Ning<sup>1</sup>

<sup>1</sup>Key Laboratory of Dark Matter and Space Astronomy, Purple Mountain Observatory, CAS, Nanjing 210023, China

<sup>2</sup>Yunnan Key Laboratory of the Solar physics and Space Science, Kunming 650216, China

<sup>3</sup>School of Earth and Space Sciences, Peking University, Beijing, 100871, China

<sup>4</sup>National Astronomical Observatories, Chinese Academy of Sciences, Beijing 100101, China

<sup>5</sup>School of Astronomy and Space Sciences, University of Chinese Academy of Sciences, Beijing 100049, China

<sup>6</sup>School of Astronomy and Space Science, Nanjing University, Nanjing 210023, China

<sup>7</sup>Key Laboratory of Modern Astronomy and Astrophysics (Nanjing University), Ministry of Education, Nanjing 210023, China

<sup>8</sup>Columbus Academy, Gahanna Ohio, OH 43230, USA

<sup>9</sup>Key Laboratory of Particle Astrophysics, Institute of High Energy Physics, CAS, Beijing 100049, China

<sup>10</sup>Yunnan Observatories, Chinese Academy of Sciences, Kunming Yunnan 650216, China

**Abstract:** Kink oscillations, which are frequently observed in coronal loops and prominences, are often accompanied by extreme-ultraviolet (EUV) waves. However, much more needs to be explored regarding the causal relationships between kink oscillations and EUV waves. In this article, we report the simultaneous detection of kink oscillations and EUV waves that are both associated with an X2.1 flare on 2023 March 03 (SOL2023-03-03T17:39). The kink oscillations, which are almost perpendicular to the axes of loop-like structures, are observed in three coronal loops and one prominence. One short loop shows in-phase oscillation within the same period of 5.2 minutes at three positions. This oscillation could be triggered by the pushing of an expanding loop and interpreted as the standing kink wave. Time lags are found between the kink oscillations of the short loop and two long loops, suggesting that the kink wave travels in different loops. The kink oscillations of one long loop and the prominence are possibly driven by the disturbance of the CME, and that of another long loop might be attributed to the interaction of the EUV wave. The onset time of the kink oscillation of the short loop is nearly same as the beginning of an EUV wave. This fact demonstrates that they are almost simultaneous. The EUV wave is most likely excited by the expanding loop structure and shows two components. The leading component is a fast coronal wave, and the trailing one could be due to the stretching magnetic field lines.

**Key words:** Coronal loops, Solar flares, Solar prominence, Solar oscillations, EUV wave, Magnetohydrodynamic (MHD)

## 1 Introduction

Kink oscillations, which are commonly observed as transverse oscillations of loop-like systems, are often perpendicular to the loop axis, non-axisymmetric, and hardly compressive in the long-wavelength regime. They are often associated with magnetohydrodynamic (MHD) waves in the solar atmosphere at multiple heights, and thus are believed to play a key role in coronal heating [1–3]. The kink-mode oscillation was first discovered as the cyclic transverse motions of coronal loop, which was shown as a large-amplitude oscillation (i.e.,  $\gg 1$  Mm) with rapid decay,

---

\* lidong@pmo.ac.cn

---

regarded as ‘decaying oscillation’ [4, 5]. The decaying kink oscillation only persists over several wave periods [6–9], and is always associated with an impulsive eruption, for instance, the decaying kink oscillation could be induced by a solar flare, a coronal jet, an extreme-ultraviolet (EUV) wave, and so on [10–12]. The decaying time  $\tau$  is roughly equal to several oscillation periods ( $P$ ), for instance, it is found that the average damping time is  $\tau = 1.79 \times P$  for large-amplitude decaying oscillations [7, 13]. On the other hand, the decayless kink oscillations, which are identified as small-amplitude ( $<1$  Mm) oscillations without significant decay, are also observed as the transverse displacement oscillations of loop-like structures [14–18]. Observations suggest that the decayless kink oscillations are persistent in solar multi-height atmospheres, for instance, they are frequently detected in coronal loops [19, 20], solar prominences [21, 22], high-temperature flare loops [23, 24], coronal bright points [25], and the sunspot [26], which could be related to their magnetic nature. The kink-mode oscillations, including decaying and decayless oscillations, are usually observed as the spatial displacement oscillations in image sequences [27–30], or they are detected as the Doppler shift oscillations in spectral lines [31, 32]. For the standing kink oscillations, their oscillation periods and loop lengths reveal a linear increasing relationship, and the oscillation periods could be measured from tens of seconds to dozens of minutes [14, 33–38]. At the same time, multiple harmonics of kink oscillations are detected in coronal loops, namely, the fundamental and second or third harmonics [39, 40], which are helpful to diagnose the density stratification of oscillating loops [41].

EUV waves, which are always observed as large-scale, fast propagating disturbances in the solar corona, are often characterized by the diffuse wavefronts with arc-shaped or circular profiles [42]. They are commonly associated with energetic eruptions such as solar flares, coronal jets, Type II radio bursts, and coronal mass ejections (CMEs), namely, the wave centers always lie closely to the epicenter of the associated eruptions [43–48]. The EUV waves are spectacular features in the solar corona, since they are coronal disturbances that can expand quickly across most fraction of the solar surface in tens of minutes, i.e., the detected propagation speeds are in the range of  $\sim 200$ – $1500$  km s $^{-1}$  with an average value of  $650$  km s $^{-1}$  [42, 49, 50]. In the Atmospheric Imaging Assembly (AIA) era [51], the study of EUV waves becomes a topic of particular interest due to their high-resolution observations [52–54]. The bright wavefronts can be clearly seen in passbands of AIA 211 Å and 193 Å, while the dark wavefronts may appear in the passband of AIA 171 Å [45]. At the same time, two components are found in the EUV wave, namely, one is the leading fast magnetosonic wave, and the other is some trailing wave-like signature [52, 55, 56]. On the other hand, the quasi-periodic, fast-mode propagating (QFP) wave trains are also investigated intensively in the AIA era, a typical QFP event consists of multiple coherent and concentric wavefronts, and thus shows the quasi periodicity of a few minutes to tens of minutes [57, 58]. Obviously, the QFP is distinguished from an EUV wave, and thus it is out scope of this study.

The kink oscillation is one of the most studied MHD waves, mainly because it is easily observed on the Sun and plays a crucial role in diagnosing plasma parameters and inferring magnetic fields in the solar atmosphere, termed as ‘MHD coronal seismology’ [59–65]. The EUV wave has also been extensively studied, largely because it could also be applied in the coronal seismology for diagnosing the coronal parameters, and provides a new tool for probing the coronal heating and particle acceleration [42, 44, 66]. Kink oscillations are usually associated with EUV waves, for instance, the transverse oscillations of coronal loops and prominences are frequently observed to be triggered by EUV waves [43, 67–70]. Those EUV waves always appear after solar flares, and then cause transverse oscillations in coronal loops or prominences. As an example, the kink oscillations are simultaneously detected in a coronal loop and a filament, both of which follow after a circular-ribbon flare [71]. Some authors [72] report an EUV wave and a kink oscillation that are simultaneously triggered by the course of jet-loop interaction. However, the simultaneous detection of kink oscillations and an EUV wave accompanied by a solar flare is rarely reported. In this paper, we investigate the driving mechanisms of kink oscillations in three coronal loops and one prominence, and a simultaneous EUV wave. The paper is organized as follows: Section 2 describes the observations, Section 3 shows our main results, Section 4 presents some discussions, and Section 5 offers a brief summary.

## 2 Observations

We analyze kink oscillations of three coronal loops and one prominence, and they are both associated with a solar flare occurred on 2023 March 03. Those solar activities were located in the active region of NOAA 13234 near the solar west limb, i.e., N21W76. They were simultaneously measured by the Atmospheric Imaging Assembly (AIA) [51] on board the Solar Dynamics Observatory (SDO), the Solar Upper Transition Region Imager (SUTRI) [73] on board the first spacecraft of the Space Advanced Technology demonstration satellite series (SATech-01), the Chinese H $\alpha$  Solar Explorer (CHASE) [74, 75], the Geostationary Operational Environmental Satellite (GOES), and the Hard

X-ray Modulation Telescope (Insight-HXMT) [76], as listed in Table 1.

Table 1. Observational instruments used in this article.

Instruments	Windows	Wavelengths	Cadence	Pixel scale	Observational time
SDO/AIA	EUV	171 Å	24 s	0.6''	17:30–18:59 UT
	EUV	193 Å			
	EUV	211 Å			
SUTRI	EUV	465 Å	~30 s	1.23''	17:45–18:40 UT
CHASE	H $\alpha$	6562.8 Å	~71 s	1.04''	17:24–17:52 UT
	H $\alpha$	6564.9 Å			
GOES	SXR	1–8 Å	1 s	–	17:39–18:20 UT
	SXR	0.5–4 Å			
HXMT/HE	HXR	100–600 keV	0.5 s	–	17:48–17:56 UT

SUTRI is designed to capture the full-Sun image at the spectral line of Ne VII 465 Å, which has a formation temperature of about 0.5 MK [77]. Each pixel scale corresponds to  $\sim 1.23''$ , and the time cadence is about 30 s. SDO/AIA provides full-disk solar maps at multiple EUV/UV channels nearly simultaneously. In this study, We use the AIA maps in three passbands of 171 Å, 193 Å, and 211 Å, corresponding to the temperatures of roughly 0.6 MK, 1.6 MK, and 2.0 MK [51], respectively. In order to avoid the saturation map, the time cadence of each AIA passband is selected as 24 s [78]. Those AIA maps have been calibrated by `aia_prep.pro`, and thus have a spatial scale of  $0.6'' \text{ pixel}^{-1}$ . CHASE acquires the spectroscopic observation in wavebands of H $\alpha$  and Fe I. In this study, we use the full-Sun spectral images at 6562.8 Å and 6564.9 Å, corresponding to the line core and wing of H $\alpha$ . They have a pixel scale of  $\sim 1.04''$  and a time cadence of  $\sim 71$  s. We also use the X-ray light curve recorded by GOES and the High Energy X-ray telescope (HE) on board Insight-HXMT, which have time cadences of 1.0 s and 0.5 s, respectively.

### 3 Results

#### 3.1 Overview

Figure 1 presents the overview of the targeted coronal loops and the associated solar flare and prominence on 2023 March 3. Panel (a) shows SXR light curves recorded by GOES at 1–8 Å (black) and 0.5–4.0 Å (blue) from 17:39 UT to 18:20 UT, indicating an X2.1-class flare. It started at  $\sim 17:39$  UT and peaked at about 17:52 UT (SolarMonitor), as marked by the vertical blue line. We notice that the HXR flux recorded by HXMT/HE (red) agrees well with the SXR derivative flux at GOES 1–8 Å (cyan), suggesting the Neupert effect [79–81] in the X2.1 flare.

Figure 1 (b) and (c) show EUV maps with a field-of-view (FOV) of about  $450'' \times 900''$  in passbands of AIA 171 Å and SUTRI 465 Å at about the SXR peak time of the X2.1 flare (i.e.,  $\sim 17:52$  UT), panels (d) and (e) present the H $\alpha$  maps with the same FOV taken by CHASE in wavelengths of 6562.8 Å and 6564.9 Å. A series of coronal loops can be seen at AIA 171 Å, and three groups of them are used to study the kink oscillations, as marked by the magenta arrows. We notice that each group appears to consist of multiple blended loops, which is impossible to be distinguished. So, they are regarded as loop systems, and their fine-scale structures are not considered. The selected loop systems seem to reveal different features, i.e., a short compact loop (L1), and two long diffuse loops (L2 and L3). It seems that those three loops root in the same region, namely, their footpoints are located closely to the X2.1 flare, as indicated by the cyan arrow. The X2.1 flare can be clearly observed in those four maps, but the coronal loops can be only seen in EUV maps. In particular, the coronal loops of L2 and L3 are not detected by SUTRI, mainly because that they are diffuse and weak. A small solar prominence can be seen underlying the long loop L3, and it shows a dark feature in passbands of AIA 171 Å and SUTRI 465 Å, but it is bright in the H $\alpha$  map observed by CHASE at 6562.8 Å, which is consistent with the low-temperature nature of the prominence [83]. Moreover, the solar prominence is likely the part of a longer loop connecting the eruption center, as indicated by the pink arrow in Figure 1 (d).

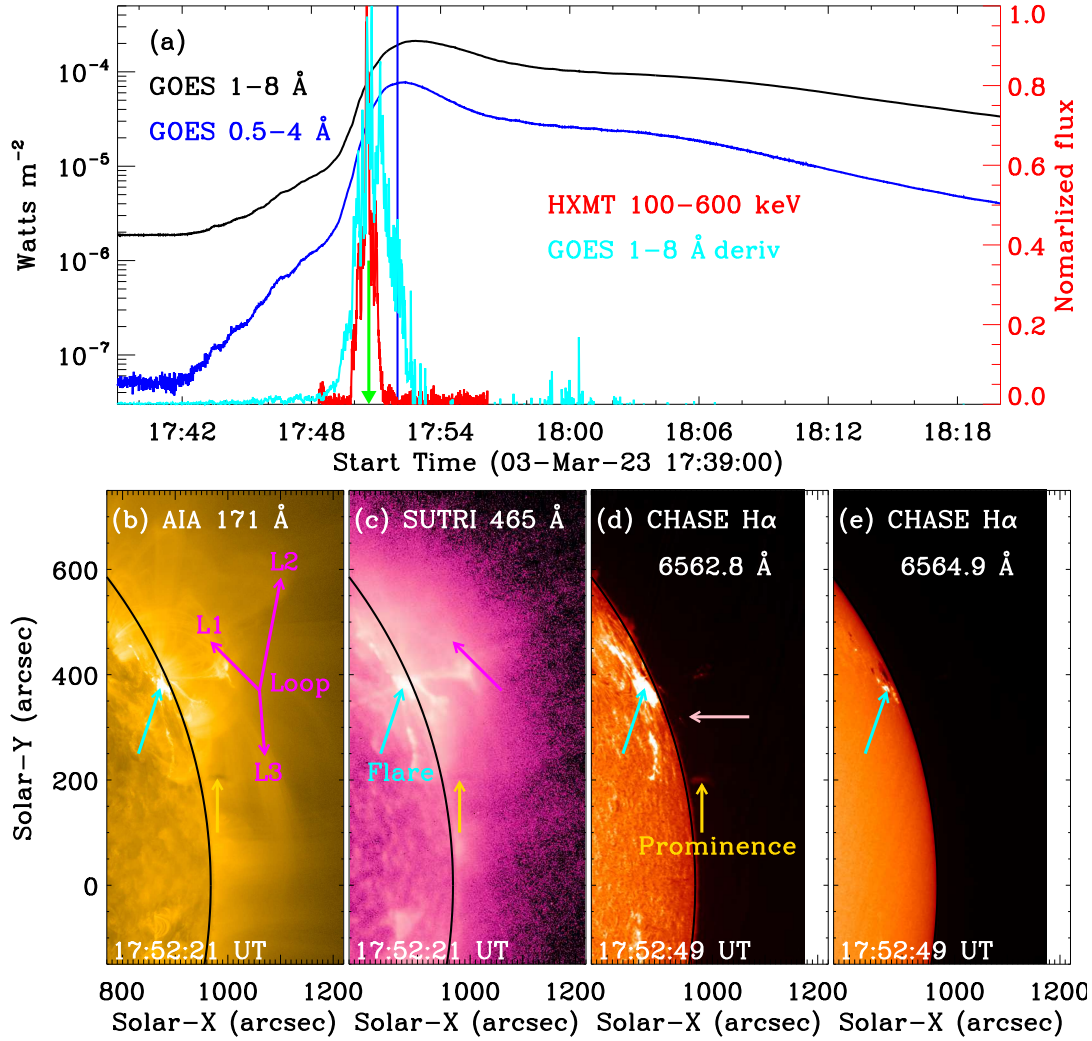


Fig. 1. Overview of the eruptive events on 2023 March 03. (a): X-ray light curves between 17:39 UT and 18:20 UT at channels of GOES 1–8 Å (black), its derivative (cyan) and 0.5–4 Å (blue), and HXMT 100–600 keV (red). The vertical blue line marks the SXR peak time of the X2.1 flare, and the green arrow indicates the HXR peak time. (b)–(e): Multi-wavelength snapshots with a FOV of  $\sim 450'' \times 900''$  measured by SDO/AIA at 171 Å (b), SUTRI at 465 Å (c), CHASE/HIS at H $\alpha$  6562.8 Å (d) and 6564.9 Å (e), respectively. The color arrows indicate the targeted coronal loops (magenta), the solar flare (cyan), the prominence (gold), and a longer but weaker loop (pink), respectively.

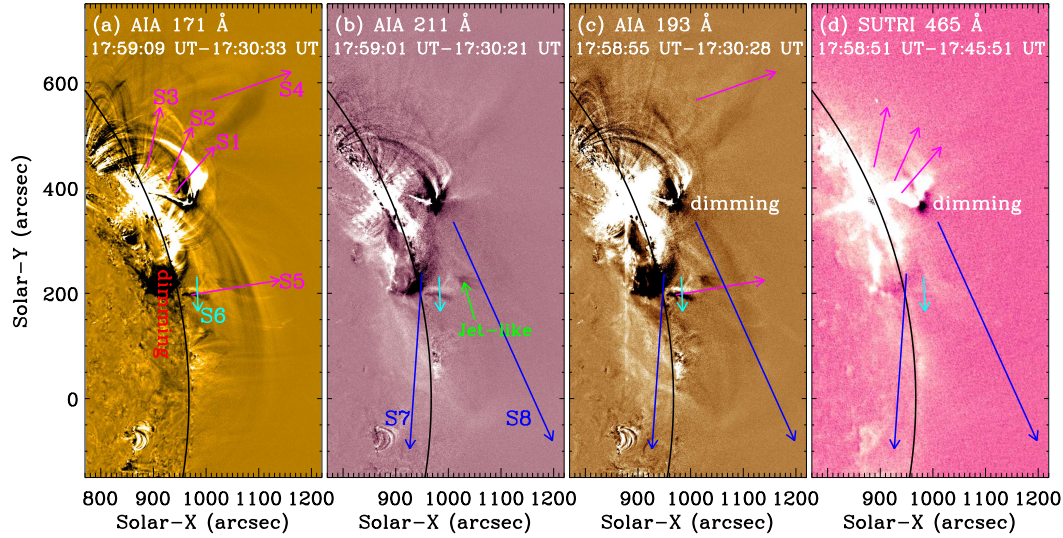


Fig. 2. Base-diffidence maps in passbands of AIA 171 Å (a), 211 Å (b) and 193 Å (c), and SUTRI 465 Å (d). The color arrows mark the locations of eight artificial slits (S1–S8), which are used to generate time-distance maps. The green arrow indicates a jet-like structure. Two animations that show the evolution of the transverse oscillations and EUV waves are available, which cover a duration of  $\sim 27$  minutes from 17:48 UT to 18:15 UT.

### 3.2 Kink oscillations

In Figure 1 (b) and (c), we can see that those coronal loops are very fuzzy, mainly because the diffuse nature of EUV emissions. In order to highlight those loops, the base-diffidence maps are derived from the origin maps, as shown in Figure 2. The coronal dimming can be simultaneously found in passbands of SUTRI 465 Å, AIA 171 Å, 211 Å, and 193 Å, and the short loop (L1) can be seen in those four maps. Two long diffuse loops can be clearly seen in the passband of AIA 171 Å, and they can also be seen at AIA 193 Å but very weak. To look closely at the appearance of transverse oscillations, five artificial straight slits (S1–S5), which are almost perpendicular to their loop axes, are chosen to generate the time-distance (TD) maps in Figures 3 and 4. The magenta arrows outline the positions and directions of those five slits. Next, one artificial straight slit (S6) that is perpendicular to the solar prominence is chosen to investigate the prominence oscillation. In order to investigate the propagation of the EUV wave, two artificial straight slits (S7 and S8) are chosen to generate the TD maps in Figure 6. In order to reduce the noise, the straight slits S1–S6 are averaged over a  $3''$  width, while the slits S7 and S8 are averaged over a width of  $30''$ . Also, a jet-like structure with the dark feature is observed at AIA 211 Å and 193 Å, as indicated by the green arrow. The online animations of `v_465.mp4` and `v_aia.mp4` show the evolution of coronal loops and prominence and the associated EUV wave during  $\sim 17:48$ – $18:15$  UT. The animations are separated because that the time resolutions of SDO/AIA and SUTRI are different.

#### 3.2.1 Loop oscillations

In this study, only the short loop (L1) has a complete loop profile, namely, the loop apex and two footpoints can be seen in passbands of AIA 171 Å and SUTRI 465 Å. Thus, three straight slits (S1–S3) that are nearly perpendicular to the loop axis are used to generate TD maps, as shown in Figure 3. Herein, the three slits are selected at the locations that are close to the loop apex (S2) and two footpoints (S1 and S3), respectively. Moreover, they are also selected at the positions where there are less overlaps with neighboring loops. In those TD maps, one can immediately notice a transverse oscillation with apparent decay. For a typical transverse oscillation, the oscillating positions are usually identified as the loop centers with the Gaussian fitting method [16, 34]. But it is difficult to use this method when some overlapping loops simultaneously exist in the TD map [14, 25, 27]. Herein, the oscillation positions are manually identified as the edge profiles of the transverse oscillation in the passband of AIA 171 Å [9, 25], as indicated by the magenta pluses ( $+$ ) in panels (a1)–(a3). Those transverse oscillations seem to decay rapidly, and thus, a sine function combined with a decaying term and a linear trend is applied to fit the observed transverse oscillation [5, 6, 9], as shown by Eq. 1:

Table 2. Fitting parameters of oscillating loops and prominence.

Slit	S1	S2	S3	S4	S5	S6
$P$ (minutes)	5.2	5.2	5.2	13.5	29.3	18.5
$\tau$ (minutes)	9.2	9.9	6.1	30.7	23.9	73.6
$A_m$ (Mm)	16.8	14.7	11.1	15.2	35.4	6.5
$v_m$ (km s <sup>-1</sup> )	338	296	223	118	127	37
$\frac{\tau}{P}$	1.8	1.9	1.2	2.3	0.8	4.0

$$A(t) = A_m \cdot \sin\left(\frac{2\pi}{P} (t - t_0) + \phi\right) \cdot e^{-\frac{(t-t_0)}{\tau}} + b \cdot (t - t_0) + C, \quad (1)$$

Here  $A_m$  denotes to an initial displacement amplitude,  $P$  and  $\tau$  represent the oscillation period and decaying time,  $t_0$ ,  $\phi$  and  $C$  refer to the onset time, initial phase and location of the decaying oscillation, while  $b$  is a constant that stands for the drifting speed of the oscillating loop in the plane-of-sky. Then, the velocity amplitude ( $v_m$ ) can be determined from the derivative of the displacement amplitude [20, 28, 38], namely,  $v_m = 2\pi \cdot \frac{A_m}{P}$ . In Figure 3, the over-plotted cyan curve in each panel represents the best-fitting result using Equation 1, which appears to match well with the oscillating skeleton of the coronal loop. Notice that the cyan curves in right panels are exactly the same as those in left panels. Table 2 (i.e., columns 2–4) shows the main fitting parameters in the transverse oscillation of the short loop at three slits.

The loop L1 shows visible transverse oscillation, as shown in Figure 3 and online animations of v\_465.mp4 and v\_aia.mp4. By seeing the associated animation, one can see that the loop L1 has a sheared shape, which is very close to the eruption center. It is pushed away by the erupting structure before the oscillation process. That is, a pushing process of the expanding loop occurs during about 17:50 UT to 17:54 UT, which is closely related to the loop oscillation. The transverse oscillation within apparent decay is most visible in the passband of AIA 171 Å, and it becomes weak but still can be seen in the passband of SUTRI 465 Å, suggesting that the oscillating loop has a multi-thermal structure. On the other hand, the decaying oscillation of loop L1 at three different slits starts at nearly the same time, and it is accompanied by the eruption of the X2.1 flare. This observational fact implies that the loop oscillates in-phase along the loop length, and thus the decaying oscillation could be in the axial fundamental mode of a standing wave. The initial oscillation amplitude also decreases when the cut slit is far away from the flare region.

The loops L2 and L3 are very diffuse, both of which shows unidirectional motions before the oscillation process, namely, the loop L2 displays a northward motion, and the loop L3 reveals a southward motion. These two loops are visible at AIA 171 Å, become weak at AIA 193 Å, and disappear at AIA 211 Å and SUTRI 465 Å, as shown in Figure 2. Therefore, Figure 4 plots TD maps for loops L2 and L3 in passbands of AIA 171 Å and 193 Å. For each loop, only one straight slit is chosen. Similar to the loop L1, the two diffuse loops exhibit transverse oscillations within apparent decay at AIA 171 Å. So we manually identify the edge profiles as the oscillating positions and fit them with Eq. 1, as shown by the magenta pluses and cyan curves. The fitting parameters are shown in Figure 2, and they match well with each other, confirming that they are decaying oscillations. In the passband of AIA 193 Å, the decaying oscillation of loop L2 becomes very weak but can be identified, but it is hard to see the decaying oscillation of loop L3, as shown in the right panels of Figure 4. The decaying oscillations of loops L2 and L3 both follow the X2.1 flare. After all, the flare SXR emissions attain their peaks earlier than the onset of the oscillations in the examined loops, as indicated by the blue line inside a red ellipse. A solar prominence appears in the TD maps at AIA 171 Å and 211 Å, as indicated by the blue arrow.

### 3.2.2 Prominence oscillations

A small prominence can be found in the solar north-west limb, which also exhibits the transverse oscillation, as shown in Figure 2 and online animations. The prominence lies in the south of the active region. It shows a southward motion before the oscillation process, and begins to oscillate after the passing of the expanding CME bubble. Figure 5 shows the TD maps at the slit S6 that is perpendicular to the prominence in passbands of AIA 171 Å, 211 Å, 193 Å, and SUTRI 465 Å. It should be pointed out that the origin maps rather than the base-diffidence maps are used to generate those TD maps, and there is not data after ~18:40 UT at SUTRI 465 Å. Those TD maps appear to reveal a transverse oscillation within at least three peaks, and they decay slowly. Similar to the oscillating loops, the oscillation positions are determined by the edge profiles of the prominence oscillation in the passband of AIA 171 Å, as indicated by the magenta pluses (+) in panel (a). Then, the observed transverse oscillation of prominence is

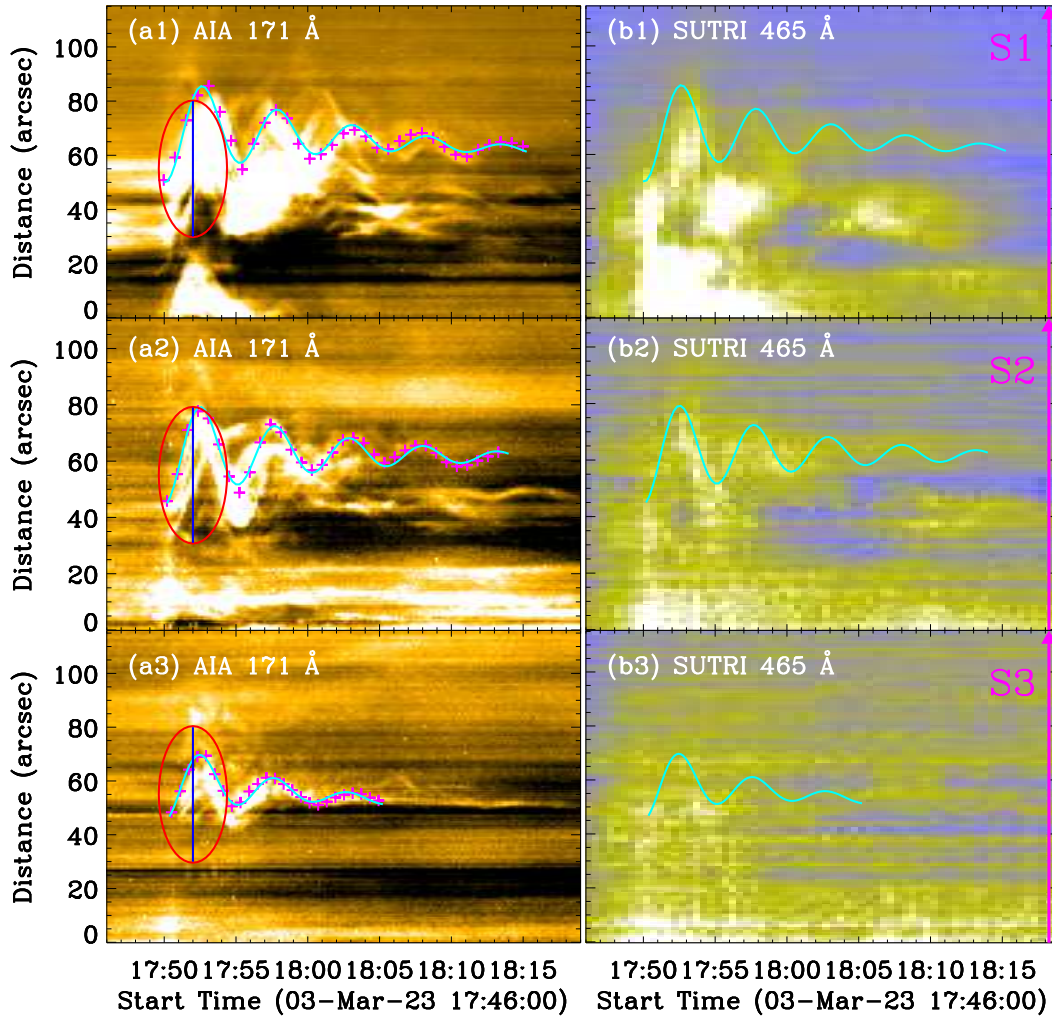


Fig. 3. TD maps showing the transverse oscillation of the short loop (L1) at three slits (S1–S3), as observed in passbands of AIA 171 Å (a1–a3) and SUTRI 465 Å (b1–b3). The magenta pluses (+) indicate the edges of the oscillating loop, whereas the cyan curves represent the best-fitting results. The blue line inside the red ellipse marks the peak time in the GOES SXR light curve. The magenta arrow outlines the slit direction.

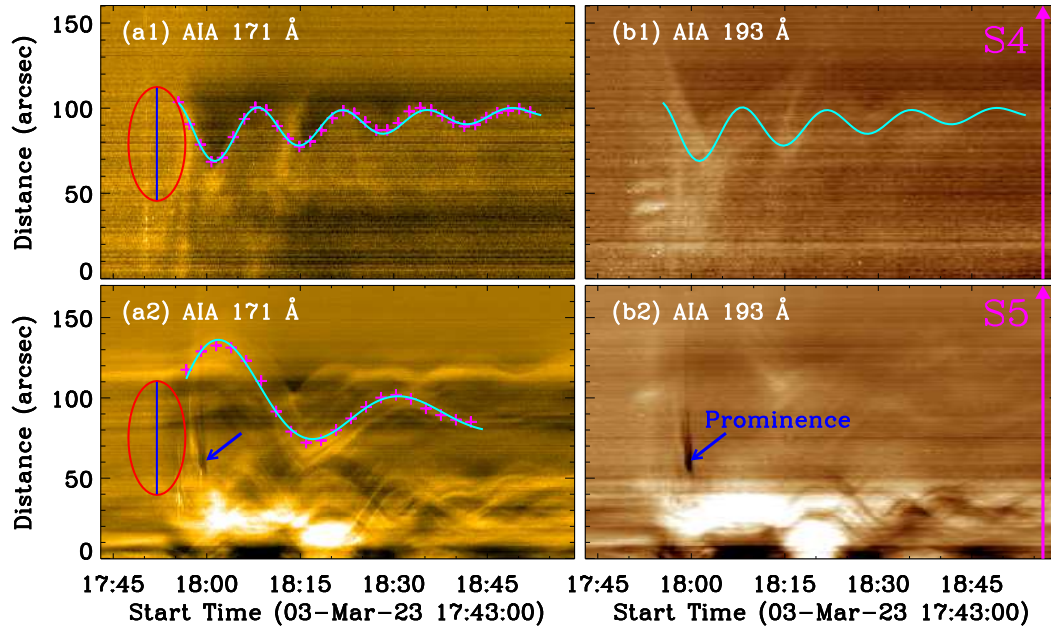


Fig. 4. Similar to Figure 3, but showing the transverse oscillations of two long loops (L2 and L3) at slits S4 and S5, respectively. The blue line inside the red ellipse marks the peak time in the GOES SXR light curve. The blue arrow indicates the prominence.

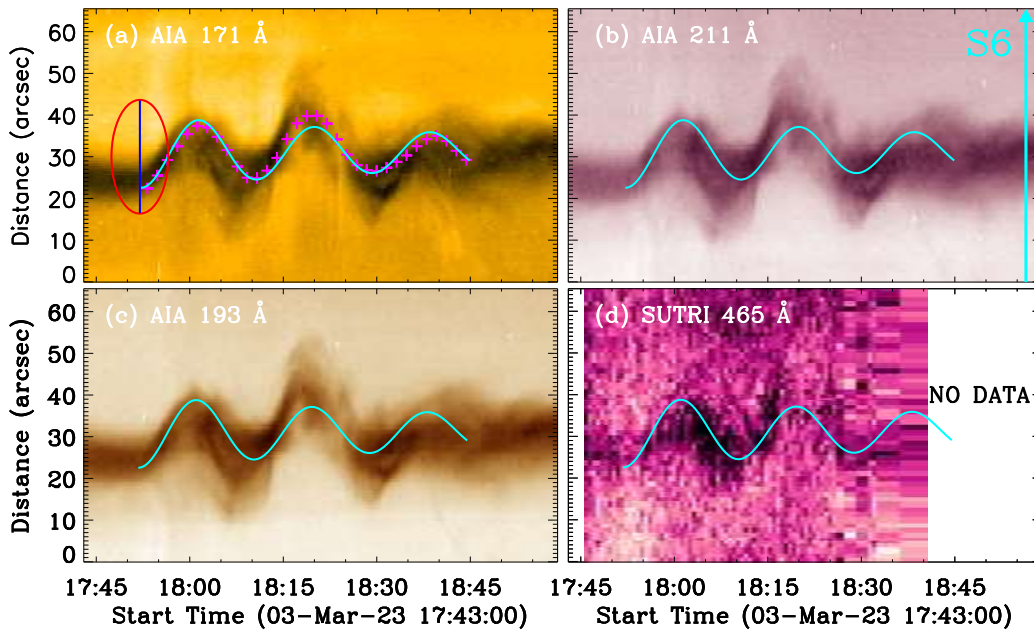


Fig. 5. TD maps showing the transverse oscillation of the prominence at the slit S6, as observed in passbands of AIA 171 Å (a), 211 Å (b), and 193 Å (c), and SUTRI 465 Å (d). The magenta pluses ('+') indicate the edges of the oscillating loop, whereas the cyan curve represent the best-fitting result. The blue line inside the red ellipse marks the peak time in the GOES SXR light curve. The cyan arrow outlines the slit direction.

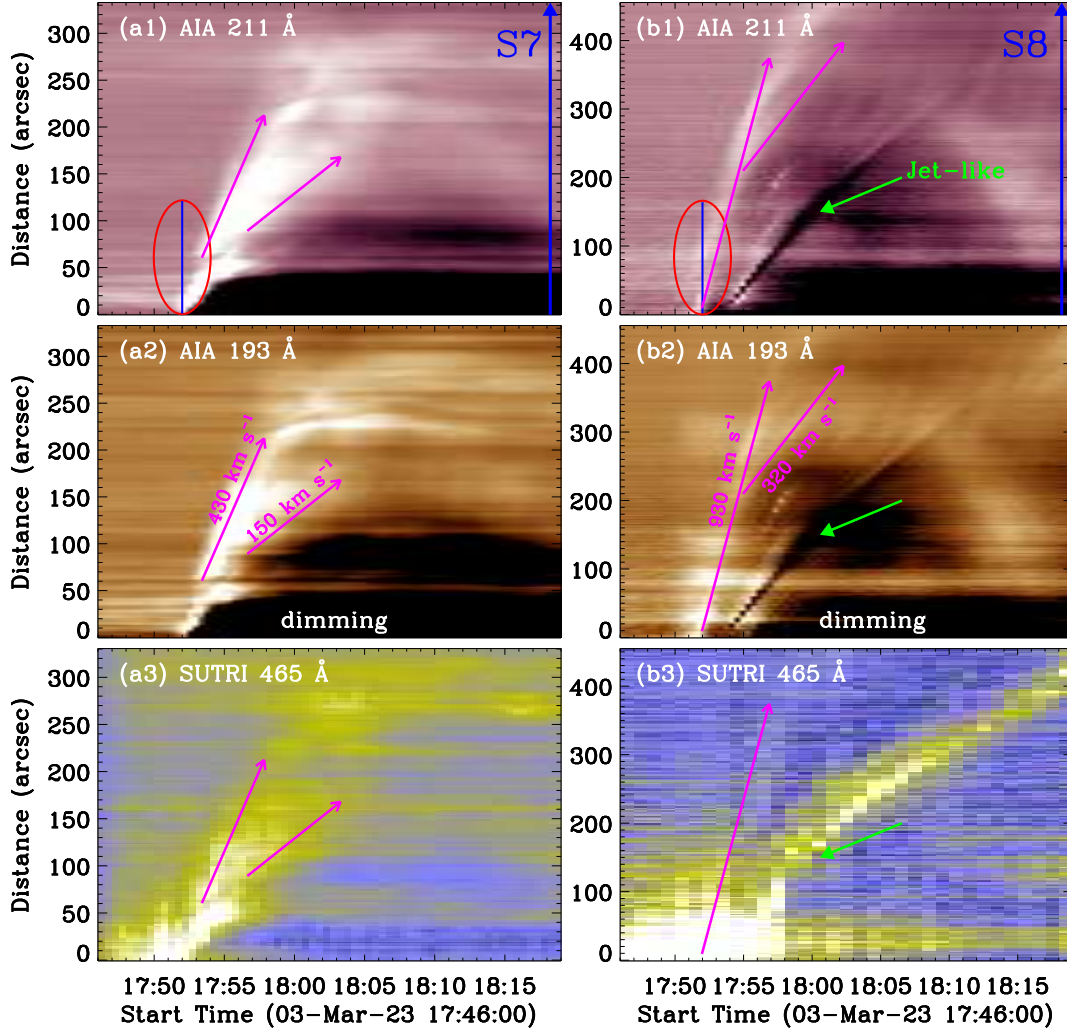


Fig. 6. TD maps showing the EUV wave at slits S7 and S8, as observed at AIA 211 Å, and 193 Å, and SUTRI 465 Å. The magenta arrows show the EUV wave, and the green arrow indicates the jet-like structure. The blue line inside the red ellipse marks the peak time in the GOES SXR light curve. The blue arrow outlines the slit direction.

fitted by using Eq. 1, and it seems to match well with the oscillating profile of the prominence, as indicated by the cyan curve in panel (a). Similarly, the decaying oscillation of the prominence is accompanied by the eruption of the X2.1 flare. Then, the fitting function (indicated by the cyan curve) is directly overplotted in TD maps at AIA 211 Å and 193 Å and SUTRI 465 Å, and it seems to agree with the prominence oscillation, as can be seen in panels (b)–(d).

### 3.3 EUV wave

The online animations of `v_465.mp4` and `v_aia.mp4` show that the X2.1 flare generates an expanding loop structure, and then excites a coronal wave-like structure propagating on the solar surface, which could be regarded as an EUV wave [44, 45]. From the online animations, we find a bright but weak wavefront after the expanding loop structure in passbands of AIA 211 Å, 171 Å, and SUTRI 465 Å, then it travels fast with the arc-shaped profile. A dark dimming region appears behind the wavefront, which could be attributed to the significant reduction of coronal densities. At the same time, a jet-like structure (indicated by the green arrow in Figure 2) is visible behind the wavefront, which might be regarded as an erupting flux rope, as can be seen in the animations.

To illustrate the evolution of the EUV wave, Figure 6 presents the TD maps at two slits (S7 and S8) that are along the EUV wave propagation. Herein, the two slits are averaged over a 30'' width, so that the bulk of this EUV wave can be covered as much as possible. Figure 6 (a1)–(a3) show the TD maps along the slit S7 that is

---

mainly inside the solar limb at AIA 211 Å, 193 Å, and SUTRI 465 Å, and they all reveal the bright inclined features, which could be the indicator of the EUV wave propagation. It is interesting that the EUV wave shows obviously two components, namely, a slow component followed by a fast one, as marked by the two magenta arrows. Then, the EUV wave velocities could be determined by the slopes of the magenta lines, which are equal to  $\sim 430 \text{ km s}^{-1}$  and  $\sim 150 \text{ km s}^{-1}$ , respectively. The velocity of the fast component is roughly three times larger than that of the slow one. Similarly, the EUV wave within two components is also detected in the TD maps along the slit S8 that is outside the solar limb, as shown in Figure 6 (b1)–(b3). Their velocities are measured to be about  $\sim 930 \text{ km s}^{-1}$  and  $\sim 320 \text{ km s}^{-1}$ , which also have a three-times difference. Here, a jet-like structure as marked by the green arrow is simultaneously seen in passbands of AIA 211 Å, 193 Å, and SUTRI 465 Å. The jet-like structure exceeds the FOV of our observational data, as shown in Figure 6 (b3), indicating that it could escape from the solar surface and propagate into the interplanetary space. We also notice that the EUV wave is accompanied by the eruption of the X2.1 flare. Also, a dark coronal dimming region appears after the eruption of the EUV wave.

## 4 Discussions

Transverse oscillations are frequently observed in coronal loops, flare loops, prominences or filaments, and even above the sunspot [7, 15, 18, 26, 27, 43, 71]. In this study, we investigate the transverse oscillations in three coronal loops, which are all associated with an X2.1 flare. They could last for several wave periods and reveal a significant decay in the displacement amplitude. The initial displacement amplitudes are measured to be in the range of  $\sim 11.1\text{--}35.4 \text{ Mm}$ , and they are found to decay rapidly. This is consistent with previous results for the decaying oscillation in coronal loops [4–6, 32]. The oscillation periods are estimated to be from about 5.2 minutes to 29.3 minutes. Such large differences of periods could be attributed to the various lengths of oscillating loops, since the oscillation periods of the standing kink wave strongly depend on their loop lengths [14, 20, 27]. The same period of 5.2 minutes is measured in the oscillating loop L1 at three different positions, and there is not apparent phase difference at those three slits, confirming that the observed transverse oscillation is indeed the fundamental mode of a standing wave. The ratio ( $\frac{\tau}{P}$ ) between the decaying time and oscillation period is measured to be about 0.8–2.3, which is similar to previous results for the decaying kink oscillations, such as an average ratio of about 1.79 [7]. All our observations suggest that the observed transverse oscillations of coronal loops are basically standing kink waves. This is different from our pervious observation, namely, the traveling kink pulse of coronal loop is initially triggered by a solar flare, and then it evolved to a standing kink wave [9]. In this study, we do not find such evolution, although both of them appear after the eruption of major flares. At the same time, the transverse oscillation is also detected in a solar prominence, and it decays slowly. The ratio between the decaying time and the oscillation period is measured to be  $\sim 4.0$ , which is close to those detected in coronal loops. Thus, it could also be interpreted as the decaying kink wave.

We also study an EUV wave, which could be excited by the expanding loop structure. The EUV wave can be simultaneously seen in passbands of AIA 211 Å, 193 Å, and SUTRI 465 Å, which agrees with previous observations [48]. We do not show the EUV wave at AIA 171 Å, because it is obscure, which might be attributed to the multiple coronal loops at AIA 171 Å, i.e., the loop L3. In agreement with previous numerical and observational results [44, 52, 55, 84], two components of the EUV wave are simultaneously observed, that is, the fast and slow components. The fast component is interpreted as the fast-mode MHD wave or the shock wave. The slow component wave-like signature is a non-wave component, and it may be induced by the reconfiguration of magnetic field lines that caused by the associated CME. It is just a visual effect caused by the disturbance resulted from the stretching magnetic field lines. A halo CME was detected to start at 18:24 UT, which could be associated with the EUV wave. The non-wave component always appears later than the fast-mode wave component. A jet-like structure appears and propagates after the EUV wave, which could be the erupting flux rope that acts as the core of the associated CME [47, 82, 85].

Both the EUV wave and decaying kink oscillations are associated with an X2.1 flare, but what is their relationship? To illustrate this issue, Figure 7 draws the time line of the studied events. The gold-shaded box represents that the period lasting from 17:45 UT to the SXR peak time of the X2.1 flare, and only the beginning parts of some kink oscillations (i.e., loops L2 and L3, and prominence) are shown, since we mainly focus on their triggers. It can be seen that the kink oscillation of the short loop L1 (black curve) first appears after the X2.1 flare eruption, which is reasonable because that the short loop L1 is closest to the flare region. Moreover, the beginning time of this kink oscillation is nearly coincident with the peak time of the HXR pulse recorded by Insight-HXMT, as marked by the green arrow. Our observation is consistent with previous findings for the decaying oscillations of coronal loops

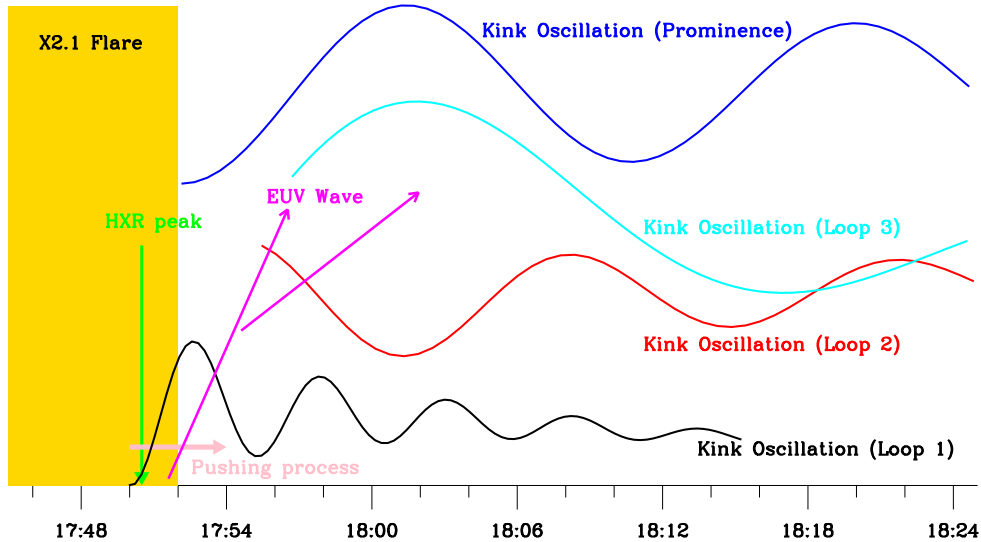


Fig. 7. Sketch of the timeline to show a plausible scenario of kink oscillations of three coronal loops (L1–L3) and one prominence, and an EUV wave, which are associated with an X2.1 flare (gold-shaded box). The green arrow marks the HXR peak time, and the pink arrow outline the pushing process of the expanding loop.

[71], implying that the trigger of kink oscillations could be associated with a strong energy release rather than the very beginning energy release via magnetic reconnection. As can be seen from the online animation, the kink oscillation of the short loop is very likely to be driven by the pushing of the expanding loop. On the other hand, the start time of kink oscillations of loops L2 and L3 (red and cyan curves) are obviously later than that of the loop L1, mainly because that those two coronal loops are far away from the flare region. This also implies that the kink wave is probably traveling in various coronal loops [9, 86]. For the kink oscillation of the long loop (L3) and the prominence, they are possibly triggered by the disturbance of the CME, because that they both start after the passing of the expanding CME bubble, and the prominence is likely the part of the long loop connecting the eruption center. The initiation of the kink oscillation of loop L2 is unclear, it might be due to the interaction of the EUV wave, although the propagation of the EUV wave in this region is very weak. However, we can find that the loop L2 shows a northward motion firstly and then begins the oscillation process, indicating that the disturbance comes from the south direction.

In Figure 7, we notice that the decaying kink oscillations and the EUV wave are almost simultaneously accompanied by the X2.1 flare, especially for the decaying kink oscillation of the loop L1, for which the excitation mechanism is unlikely to involve the EUV wave as an intermediary. This is different from previous observations, for instance, the EUV waves triggered by solar flares often result in transverse oscillations of the remote coronal loops and prominences or filaments when they propagate across those loop-like structures [12, 43, 70, 87, 88]. However, we do not find such relationship between kink oscillations and EUV waves, suggesting that their triggered sources are same, i.e., the expanding loop structure associated with the X2.1 flare.

## 5 Summary

Using the imaging observations measured by SUTRI, SDO/AIA, and CHASE, combined with the X-ray light curves recorded by GOES and Insight-HXMT, we investigate flare-associated kink oscillations and EUV waves, and the objective being to shed more light on the broad subject as to how low-frequency waves are excited in the solar atmosphere. Our main conclusions are summarized as follows:

- (1) The decaying kink oscillations and the EUV wave are simultaneously observed in passbands of AIA 171 Å, 193 Å, 211 Å, and SUTRI 465Å, and they are all associated with an X2.1 flare.
- (2) The decaying kink oscillations are found in three coronal loops and one solar prominence, and they can be interpreted as the standing kink waves. The kink oscillation of the loop L1 is identified as an axial fundamental kink mode, and it could be driven by the pushing of the expanding loop. The kink oscillations of the loop L3 and the

---

prominence are possibly excited by the disturbance of the CME, and the kink oscillation of the loop L2 might be due to the interaction of the EUV wave.

(3) Two component EUV wave-like structures are simultaneously observed in passbands of AIA 211 Å and 193 Å, and SUTRI 465Å. Their speed ratio is roughly equal to three. The fast component could be a fast-mode MHD wave, which should be driven by the lateral rapid expansion of the erupting loops. The slow component is non-wave component, which might be just a visual effect caused by the disturbance resulted from the stretching magnetic field lines.

(4) A jet-like structure is observed to propagate after the EUV wave, which could be regarded as the erupting flux rope that acts as the core of the CME.

## Acknowledgements

We thank the two referees for their constructive suggestions and detailed comments. This work was supported by the National Key R&D Program of China 2021YFA1600502 (2021YFA1600500), NSFC under grants 11973092, 12073081, 12003064, 12333009. D. Li is also supported by the Surface Project of Jiangsu Province under the grant BK20211402 and Yunnan Key Laboratory of Solar Physics and Space Science (202205AG070009) under the grant YNSPCC202207. SUTRI is a collaborative project conducted by the National Astronomical Observatories of CAS, Peking University, Tongji University, Xi'an Institute of Optics and Precision Mechanics of CAS and the Innovation Academy for Microsatellites of CAS. The CHASE mission is supported by China National Space Administration (CNSA).

## References

- 1 Van Doorselaere, T., Srivastava, A. K., Antolin, P., et al. 2020, *Space Sci. Rev.*, 216, 140.
- 2 Nakariakov, V. M., Anfinogentov, S. A., Antolin, P., et al. 2021, *Space Sci. Rev.*, 217, 73.
- 3 Chelpanov, M., Anfinogentov, S., Kostarev, D., et al. 2022, *Solar-Terrestrial Physics*, 8, 3.
- 4 Aschwanden, M. J., Fletcher, L., Schrijver, C. J., et al. 1999, *Astrophys. J.*, 520, 880.
- 5 Nakariakov, V. M., Ofman, L., Deluca, E. E., et al. 1999, *Science*, 285, 862.
- 6 Su, W., Guo, Y., Erdélyi, R., et al. 2018, *Scientific Reports*, 8, 4471.
- 7 Nechaeva, A., Zimovets, I. V., Nakariakov, V. M., et al. 2019, *Astrophys. J. Suppl.*, 241, 31.
- 8 Kumar, P., Nakariakov, V. M., Karpen, J. T., et al. 2022, *Astrophys. J. Lett.*, 932, L9.
- 9 Li, D., Bai, X., Tian, H., et al. 2023, *Astron. Astrophys.*, 675, A169.
- 10 Zimovets, I. V. & Nakariakov, V. M. 2015, *Astron. Astrophys.*, 577, A4.
- 11 Reeves, K. K., Polito, V., Chen, B., et al. 2020, *Astrophys. J.*, 905, 165.
- 12 Zhang, Q., Li, C., Li, D., et al. 2022, *Astrophys. J. Lett.*, 937, L21.
- 13 Nakariakov, V. M. & Yelagandula, N. V. 2023, *Universe*, 9, 95.
- 14 Anfinogentov, S. A., Nakariakov, V. M., & Nisticò, G. 2015, *Astron. Astrophys.*, 583, A136.
- 15 Li, D., Li, Y., Lu, L., et al. 2020, *Astrophys. J. Lett.*, 893, L17.
- 16 Mandal, S., Tian, H., & Peter, H. 2021, *Astron. Astrophys.*, 652, L3.
- 17 Shi, F., Ning, Z., & Li, D. 2022, *Research in Astronomy and Astrophysics*, 22, 105017.
- 18 Zhong, S., Nakariakov, V. M., Kolotkov, D. Y., et al. 2023, *Nature Communications*, 14, 5298.
- 19 Safna Banu, K., Murya, R. A., & Jain Jacob, P. T. 2022, *Sol. Phys.*, 297, 134.
- 20 Li, D. & Long, D. M. 2023, *Astrophys. J.*, 944, 8.
- 21 Arregui, I., Oliver, R., & Ballester, J. L. 2018, *Living Rev. Sol. Phys.*, 15, 3.
- 22 Li, D., Shen, Y., Ning, Z., et al. 2018, *Astrophys. J.*, 863, 192.
- 23 Li, D., Yuan, D., Su, Y. N., et al. 2018, *Astron. Astrophys.*, 617, A86.
- 24 Shi, M., Li, B., Chen, S.-X., et al. 2023, *Astrophys. J. Lett.*, 943, L19.
- 25 Gao, Y., Tian, H., Van Doorselaere, T., et al. 2022, *Astrophys. J.*, 930, 55.
- 26 Yuan, D., Fu, L., Cao, W., et al. 2023, *Nature Astronomy*.
- 27 Goddard, C. R., Nisticò, G., Nakariakov, V. M., et al. 2016, *Astron. Astrophys.*, 585, A137.
- 28 Li, D., Xue, J., Yuan, D., et al. 2022, *Science China Physics, Mechanics, and Astronomy*, 65, 239611.
- 29 Li, D., Shi, F., Zhao, H., et al. 2022, *Frontiers in Astronomy and Space Sciences*, 9, 1032099.
- 30 Guo, X., Liang, B., Feng, S., et al. 2022, *Research in Astronomy and Astrophysics*, 22, 115012.
- 31 Tian, H., McIntosh, S. W., Wang, T., et al. 2012, *Astrophys. J.*, 759, 144.
- 32 Li, D., Ning, Z. J., Huang, Y., et al. 2017, *Astrophys. J.*, 849, 113.
- 33 Ning, Z., Wang, Y., Hong, Z., et al. 2022, *Sol. Phys.*, 297, 2.
- 34 Zhong, S., Nakariakov, V. M., Kolotkov, D. Y., et al. 2022, *Monthly Notices of the Royal Astronomical Society*, 516, 5989.
- 35 Zhong, S., Nakariakov, V. M., Miao, Y., et al. 2023, *Scientific Reports*, 13, 12963.
- 36 Li, D. 2022, *Science in China E: Technological Sciences*, 65, 139.
- 37 Gao, Y., Guo, M., Van Doorselaere, T., et al. 2023, *Astrophys. J.*, 955, 73.
- 38 Petrova, E., Magyar, N., Van Doorselaere, T., et al. 2023, *Astrophys. J.*, 946, 36.
- 39 Duckenfield, T. J., Goddard, C. R., Pascoe, D. J., et al. 2019, *Astron. Astrophys.*, 632, A64.
- 40 Zhang, Q., Zhou, Y., Li, C., et al. 2023, *Astrophys. J.*, 951, 126.
- 41 Andries, J., Arregui, I., & Goossens, M. 2005, *Astrophys. J. Lett.*, 624, L57.

- 
- 42 Shen, Y., Zhou, X., Duan, Y., et al. 2022, *Sol. Phys.*, 297, 20.  
43 Asai, A., Ishii, T. T., Isobe, H., et al. 2012, *Astrophys. J. Lett.*, 745, L18.  
44 Liu, W. & Ofman, L. 2014, *Sol. Phys.*, 289, 3233.  
45 Warmuth, A. 2015, *Living Rev. Sol. Phys.*, 12, 3.  
46 Zheng, R., Xue, Z., Chen, Y., et al. 2019, *Astrophys. J.*, 871, 232.  
47 Shen, Y. 2021, *Proceedings of the Royal Society of London Series A*, 477, 217.  
48 Hou, Z., Tian, H., Su, W., et al. 2023, *Astrophys. J.*, 953, 171.  
49 Nitta, N. V., Schrijver, C. J., Title, A. M., et al. 2013, *Astrophys. J.*, 776, 58.  
50 Liu, Y., Zheng, R., Zhang, L., et al. 2023, *Astron. Astrophys.*, 674, A167.  
51 Lemen, J. R., Title, A. M., Akin, D. J., et al. 2012, *Sol. Phys.*, 275, 17.  
52 Chen, P. F. & Wu, Y. 2011, *Astrophys. J. Lett.*, 732, L20.  
53 Shen, Y. & Liu, Y. 2012, *Astrophys. J.*, 754, 7.  
54 Shen, Y. & Liu, Y. 2012, *Astrophys. J. Lett.*, 752, L23.  
55 Shen, Y., Ichimoto, K., Ishii, T. T., et al. 2014, *Astrophys. J.*, 786, 151.  
56 Sun, Z., Tian, H., Chen, P. F., et al. 2022, *Astrophys. J. Lett.*, 939, L18.  
57 Wang, J., Yan, X., Xue, Z., et al. 2022, *Astrophys. J. Lett.*, 936, L12.  
58 Zhou, X., Shen, Y., Liang, H., et al. 2022, *Astrophys. J.*, 941, 59.  
59 Yuan, D. & Van Doorsselaere, T. 2016, *Astrophys. J. Suppl.*, 223, 23.  
60 Yuan, D. & Van Doorsselaere, T. 2016, *Astrophys. J. Suppl.*, 223, 24.  
61 Yuan, D., Li, B., & Walsh, R. W. 2016, *Astrophys. J.*, 828, 17.  
62 Yang, Z., Tian, H., Tomczyk, S., et al. 2020, *Science in China E: Technological Sciences*, 63, 2357.  
63 Yang, Z., Bethge, C., Tian, H., et al. 2020, *Science*, 369, 694.  
64 Anfinogentov, S. A., Antolin, P., Inglis, A. R., et al. 2022, *Space Sci. Rev.*, 218, 9.  
65 Kolotkov, D. Y., Li, B., & Leibacher, J. 2023, *Sol. Phys.*, 298, 40.  
66 Zheng, R., Liu, Y., Liu, W., et al. 2023, *Astrophys. J. Lett.*, 949, L8.  
67 Liu, R., Liu, C., Xu, Y., et al. 2013, *Astrophys. J.*, 773, 166.  
68 Shen, Y., Liu, Y. D., Chen, P. F., et al. 2014, *Astrophys. J.*, 795, 130.  
69 Zhang, Q. M. & Ji, H. S. 2018, *Astrophys. J.*, 860, 113.  
70 Devi, P., Chandra, R., Awasthi, A. K., et al. 2022, *Sol. Phys.*, 297, 153.  
71 Zhang, Q. M. 2020, *Astron. Astrophys.*, 642, A159.  
72 Shen, Y., Tang, Z., Li, H., et al. 2018, *Monthly Notices of the Royal Astronomical Society*, 480, L63.  
73 Bai, X., Tian, H., Deng, Y., et al. 2023, *Research in Astronomy and Astrophysics*, 23, 065014.  
74 Li, C., Fang, C., Li, Z., et al. 2022, *Science China Physics, Mechanics, and Astronomy*, 65, 289602.  
75 Li, C., Tian, H., Huang, Y., et al. 2023, *Science in China E: Technological Sciences*, 66, 1203.  
76 Zhang, S.-N., Li, T., Lu, F., et al. 2020, *Science China Physics, Mechanics, and Astronomy*, 63, 249502.  
77 Tian, H. 2017, *Research in Astronomy and Astrophysics*, 17, 110.  
78 Li, D., Ning, Z. J., & Zhang, Q. M. 2015, *Astrophys. J.*, 807, 72.  
79 Neupert, W. M. 1968, *Astrophys. J. Lett.*, 153, L59.  
80 Ning, Z. 2008, *Sol. Phys.*, 248, 99.  
81 Ning, Z. 2009, *Science in China: Physics, Mechanics and Astronomy*, 52, 1686.  
82 Shen, Y., Qu, Z., Zhou, C., et al. 2019, *Astrophys. J. Lett.*, 885, L11.  
83 Parenti, S. 2014, *Living Rev. Sol. Phys.*, 11, 1.  
84 Chen, P. F., Wu, S. T., Shibata, K., et al. 2002, *Astrophys. J. Lett.*, 572, L99.  
85 Shen, Y., Qu, Z., Yuan, D., et al. 2019, *Astrophys. J.*, 883, 104.  
86 Li, B., Guo, M., Yu, H., et al. 2023, *Monthly Notices of the Royal Astronomical Society*, 518, L57.  
87 Shen, Y., Liu, Y., Tian, Z., et al. 2017, *Astrophys. J.*, 851, 101.  
88 Xue, Z. K., Yan, X. L., Qu, Z. Q., et al. 2014, *Solar Polarization* 7, 489, 53